Journal of Instrumentation

SISSA

PAPER • **OPEN ACCESS**

A study on energy window-based scatter correction methods in ^{99m}Tc and ^{123}I imaging

To cite this article: M. Can *et al* 2023 *JINST* **18** P10009

View the article online for updates and enhancements.

You may also like

- ^{177}Lu SPECT imaging in the presence of ^{90}Y: does ^{90}Y degrade image quantification? a simulation study
Cassandra Miller, Carlos Uribe, Xinchi Hou et al.
- The influence of triple energy window scatter correction on activity quantification for ^{177}Lu molecular radiotherapy
Andrew P Robinson, Jill Tipping, David M Cullen et al.
- Septal penetration correction in I-131 imaging following thyroid cancer treatment
Fiona Barrack, James Scuffham and Sarah McQuaid

This content was downloaded from IP address 194.27.104.230 on 02/11/2023 at 11:08

Jinst

Published by IOP Publishing for Sissa Medialab

Received: *May 9, 2023*
Accepted: *August 29, 2023*
Published: *October 9, 2023*

A study on energy window-based scatter correction methods in ^{99m}Tc and ^{123}I imaging

M. Can,[a,b,*] **Ö. Karadeniz,**[c,b] **G. Çapa Kaya**[d,b] **and T. Ertay**[d,b]

[a] *Program of Nuclear Medicine Techniques, Vocational School of Health Services, Dokuz Eylul University, İzmir, Turkey*
[b] *Department of Medical Physics, Institute of Health Sciences, Dokuz Eylul University, İzmir, Turkey*
[c] *Department of Physics, Faculty of Sciences, Dokuz Eylul University, İzmir, Turkey*
[d] *Department of Nuclear Medicine, Faculty of Medicine, Dokuz Eylul University, İzmir, Turkey*

E-mail: melek.can@deu.edu.tr

Abstract: Tc-99m and I-123 are radionuclides commonly used for diagnostic examination in nuclear medicine. Detection of the scattered photons by the Compton interactions in the photopeak energy window is a factor affecting the image quality. DEW and TEW scatter correction methods are used to improve the image quality degrade by Compton scattered photons. In the study, planar and SPECT images of sphere, rod and cardiac phantom containing different activities were acquired with a gamma camera system. DEW/TEW corrected and uncorrected images for Tc-99m/I-123 were evaluated qualitatively and quantitatively. Both for planar and SPECT images, the DEW and TEW scatter correction methods were found to improve the image quality at varying rates.

Keywords: Compton imaging; Gamma camera, SPECT, PET PET/CT, coronary CT angiography (CTA); Image reconstruction in medical imaging; Medical-image reconstruction methods and algorithms, computer-aided diagnosis

*Corresponding author.

© 2023 The Author(s). Published by IOP Publishing Ltd on behalf of Sissa Medialab. Original content from this work may be used under the terms of the Creative Commons Attribution 4.0 licence. Any further distribution of this work must maintain attribution to the author(s) and the title of the work, journal citation and DOI.

https://doi.org/10.1088/1748-0221/18/10/P10009

2023 JINST 18 P10009

Contents

1 Introduction **1**

2 Materials and methods **2**
- 2.1 Imaging system and collimators 2
- 2.2 Preparation of phantoms 3
- 2.3 Imaging and acquisition parameters 3
- 2.4 Energy-based scatter correction methods 4
  - 2.4.1 Dual-energy window (DEW) scatter correction method 4
  - 2.4.2 Triple-energy window (TEW) scatter correction method 4
- 2.5 Evaluation of image quality 5
  - 2.5.1 Region of interest (ROI) 5
  - 2.5.2 Image contrast 6
  - 2.5.3 Spatial resolution 7

3 Results and discussion **7**
- 3.1 Tc-99m energy spectrum 7
- 3.2 I-123 energy spectrum 9
- 3.3 Evaluation of DEW/TEW methods on planar imaging 10
  - 3.3.1 Visual evaluations 10
  - 3.3.2 Image quality parameters 11
- 3.4 Evaluation of DEW/TEW methods on SPECT imaging 14
  - 3.4.1 Visual evaluations 14
  - 3.4.2 Image quality parameters 15

4 Conclusion **17**

1 Introduction

Over the years, Technetium-99m (^{99m}Tc) imaging has been routinely performed for diagnostic examination in nuclear medicine. Tc-99m is a radionuclide used in clinical imaging, such as dynamic and cortical kidney scintigraphy, myocardial perfusion scintigraphy, bone marrow scintigraphy, and gastric emptying function evaluation. It is mentioned that Tc-99m's short half-life (6 hours), emitting low-energy (140 keV) photons, and non-alpha or beta emission make ^{99m}Tc the most widely used radionuclide [1].

Another radionuclide used in nuclear medicine is Iodine-123 (^{123}I), has a half-life of 13.22 hours. This radiopharmaceutical is used for ^{123}I metaiodobenzylguanidine (MIBG) scintigraphy in order to the assessment of sympathetic cardiac function, thyroid scintigraphy uptake measurements, and the evaluation of fatty acid metabolism of the myocardium. As ^{123}I decays to Tellurium-123 (^{123}Te)

2023 JINST 18 P10009

by electron capture, it emits a gamma photon with an energy of 159 keV (83%), which is used basically in ^{123}I imaging. Otherwise, this isotope also emits another photon with an energy of 529 keV (1.39%) [2, 3].

In ^{99m}Tc imaging, although the photoelectric effect is the most common interaction for the 140 keV energy photons, Compton scattering also occurs in patient tissue. Such that, in ^{99m}Tc imaging, approximately 30% of the photons detected in the primary energy window can arise from Compton scattered photons [4–6]. Therefore, one of the major problems in both planar and SPECT imaging is detection of these Compton-scattered photons degrade image quality by carrying misleading information about the photon's emission point [7–10].

As for ^{123}I imaging, except for 159 keV gamma rays, other gamma rays are not used in nuclear medicine imaging due to their low abundance of decay. However, these high-energy gamma rays are the main source of penetration and scattering [3, 11–14]. Namely, high energy photons penetrate through the collimator, these penetrated high-energy photons cross the crystal and Compton-scattered in the electronic elements behind the crystal. When scattered photons re-enter the crystal, they are detected in the photopeak window because of their lower energy [12, 14]. It is mentioned that the total amount of the penetrated high-energy photons in the photopeak window could be 49%–60% of the detected photons [15]. Different publications have emphasized that these penetration and scatter events degrade image quality [2, 3, 10, 11, 16].

Therefore, various scatter correction methods are suggested by several investigators to decrease the contribution of Compton-scattered photons affecting the quantitative and qualitative accuracy of the images [3, 7, 8, 13, 17–21]. Commonly used scatter correction methods in nuclear medicine imaging systems are dual-energy window (DEW), triple-energy window (TEW, trapezoidal and triangular approximation), dual-photopeak window (DPW), photopeak energy distribution analysis (PEDA), channel ratio (CRM), and downscatter correction.

DEW and TEW methods are the most widely used scatter correction methods for ^{99m}Tc and ^{123}I imaging, respectively [17, 22]. These long-used methods in gamma spectroscopic measurements are a spectral analysis approaches based on subtracting the scatter energy windows, set on the Compton region of the spectrum, from the net peak area [18, 20, 21]. Many phantom and simulation studies on the DEW/TEW scatter correction methods in ^{99m}Tc/^{123}I imaging have been conducted and concluded that the scatter correction methods enhance image quality in both planar and SPECT images [2, 3, 7, 9, 13, 17, 19, 22–27].

In this paper, the results of a study on the DEW/TEW scatter correction applications in ^{99m}Tc and ^{123}I imaging is presented and the effect of these methods in planar and SPECT images were evaluated in terms of image quality parameters.

2 Materials and methods

2.1 Imaging system and collimators

In this study, acquisitions were performed with a dual-headed General Electric (GE) Healthcare (Optima NM/CT 640) gamma camera (figure 1). The system was equipped with a NaI(Tl) scintillation crystal (thickness of 9.5 mm) and 59 photomultiplier tubes (53 of diameter of 76 mm and 6 of diameter of 38 mm) per detector. The low energy-high resolution (LEHR), medium energy-general

2023 JINST 18 P10009

purpose (MEGP) and high energy-general purpose (HEGP) collimators, as supplied by gamma camera manufacturers, were used for measurements. The hole shape of these collimators is hexagonal. The design parameters of the collimators are provided in table 1.

Table 1. Collimator specifications. LEHR: Low-energy high resolution. MEGP: Medium-energy general purpose. HEGP: High-energy general purpose.

Collimator	Hole diameter (mm)	Hole length (mm)	Septal thickness (mm)
LEHR	1.50	35	0.20
MEGP	3.00	58	1.05
HEGP	4.00	66	1.80



Figure 1. GE Healthcare, Optima NM/CT 640 SPECT/CT.

2.2 Preparation of phantoms

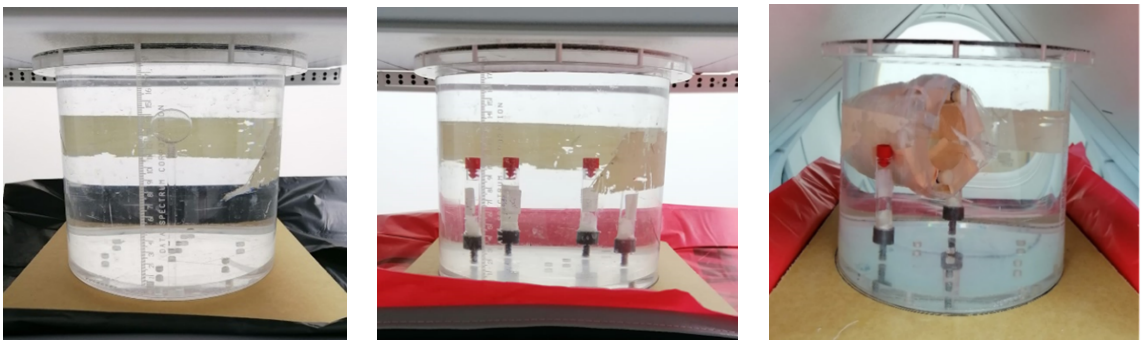
A fillable sphere (15.3 ml), rods (diameter of 1 cm) and cardiac insert phantom (240 ml) inside the Jaszczak SPECT phantom (diameter of 21.6 cm, height of 18.6 cm, cylinder wall thickness of 3.2 mm) were filled with ^{99m}Tc and ^{123}I radiopharmaceutical solutions (figure 2). The cardiac phantom is fixed into the Jaszczak phantom by reference to the heart position in nuclear medicine myocardial imaging.

2.3 Imaging and acquisition parameters

Planar imaging was performed using one of the two gamma camera detectors and acquired on a 256×256 matrix, with a 1.33 zoom for ^{99m}Tc and 1.46 zoom for ^{123}I (pixel size of 1.46 mm). Acquisition time of 360 seconds was set for planar imaging.

Additionally, phantoms were scanned by SPECT acquisition over 360° at 30° view angle (25 sec per angle, step and shoot mode) in a 64×64 matrix size with a 1.33 zoom. SPECT images were

2023 JINST 18 P10009



(a) (b) (c)

Figure 2. A fillable (a) sphere, (b) rods and (c) cardiac insert phantom inside the Jaszczak SPECT phantom.

reconstructed using an iterative ordered-subsets expectation maximization (OSEM) reconstruction algorithm with two iterations and 10 subsets, as provided by the imaging system software (Xeleris® 4.0 Processing&Review workstation).

2.4 Energy-based scatter correction methods

2.4.1 Dual-energy window (DEW) scatter correction method

The dual-energy window (DEW) method is the first scatter correction method, which was proposed by Jaszczak [6, 7]. This is the simplest energy-based correction method and applied for both SPECT and PET images. The DEW method uses two adjacent energy windows, one photopeak and the other scattering. It is assumed that both energy windows contain scattered and unscattered coincidences [6]. Namely, the spatial distribution of the counts recorded in a lower scatter window placed in Compton region of the energy spectrum is the same as the spatial distribution of the scatter counts recorded in the photopeak window [21]. Therefore, the counts recorded with the scatter window are used to estimate the scattered photons included in the main photopeak window, as shown in figure 3(a). Then, the primary photon (unscattered) counts (C_{prim}) can be obtained by subtraction of the scattered photon counts (C_{sca}) from the total count (C_{tot}). This formula is given as follows [8]:

$$C_{\text{prim}} = C_{\text{tot}} - C_{\text{sca}} \tag{2.1}$$

The energy window-sets used in this study were chosen from results of the similar studies [2, 8, 23, 25]. Accordingly, five different energy windows for DEW scatter correction method in $^{99\text{m}}$Tc imaging were studied.

2.4.2 Triple-energy window (TEW) scatter correction method

The TEW method is another energy-based scatter correction method utilized in gamma camera imaging. The spectral representation of the TEW method using trapezoidal approximation is shown in figure 3(b). In this method, the trapezoidal area formed by the narrow scatter windows (W_s) placed on the left and right sides of the photopeak window is used to estimate the Compton scattering contribution in the photopeak energy spectrum [17]. The C_{sca} is referred to counts of windows (C_{left} and C_{right}) on both sides of the photopeak window. The W_m and W_s are defined as the width of the

2023 JINST 18 P10009

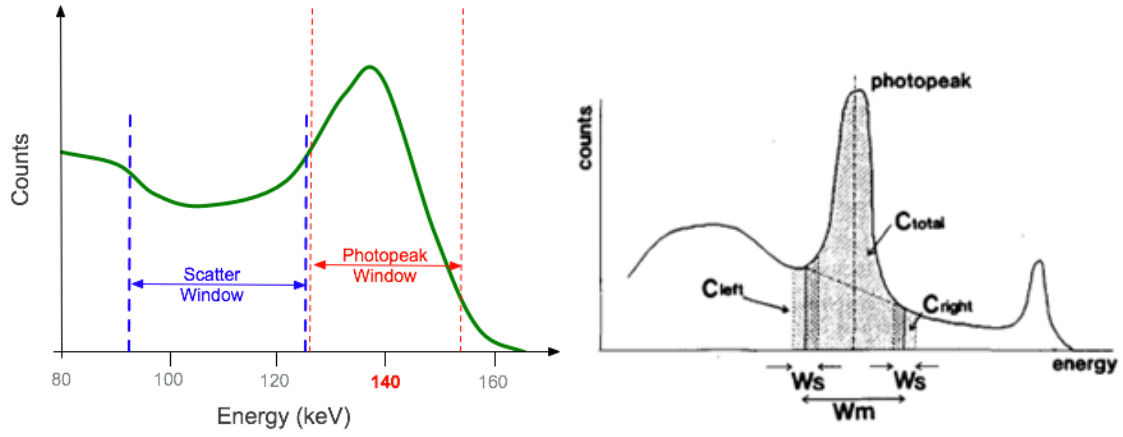


Figure 3. (a) Illustration of DEW correction method on the Tc-99m energy spectrum [36]. Public Domain. (b) Spectral representation of TEW correction method using trapezoidal approximation. Reproduced from [35]. CC BY 3.0.

photopeak (main) and scatter windows, respectively. Then, the scatter counts (C_{sca}) can be expressed by the following formula [8, 17, 19]:

$$C_{\text{sca}} \cong \left(\frac{C_{\text{left}}}{W_s} + \frac{C_{\text{right}}}{W_s}\right) \cdot \left(\frac{W_m}{2}\right) \tag{2.2}$$

$$C_{\text{prim}} = C_{\text{tot}} - \left(\frac{C_{\text{left}}}{W_s} + \frac{C_{\text{right}}}{W_s}\right) \cdot \left(\frac{W_m}{2}\right) \tag{2.3}$$

In the study, based on the findings of related studies, four different energy window sets were chosen for the TEW corrected ^{123}I imaging [3, 17, 19, 28].

2.5 Evaluation of image quality

The image qualities of the scatter corrected planar and SPECT images were quantitatively evaluated using the traditional image quality parameters of contrast and spatial resolution.

2.5.1 Region of interest (ROI)

In nuclear imaging, a region of interest (ROI) is a closed boundary superimposed on the image, which refers the exact area corresponding to the radioactive source in the image. As the total counts in all pixels of the ROI is a measure of the activity uptake, the choice of the ROI is the most essential factor when considering image quality parameters. It might be drawn manually or automatically by the computer [29, 30].

In this study, the circular source ROIs were carefully drawn on the planar sphere and rods images, paying attention to comprise a total activity region. The background (BG) ROIs were drawn on the planar images also, and care has been made to ensure that the number of pixels in the source and BG ROIs were the same (figure 4(a–d)).

In SPECT images of the cardiac phantom, three source ROIs were drawn on the short-axis slices of the myocardium, whereas BG ROIs were drawn from the region without activity uptake(figure 4(e,f)).

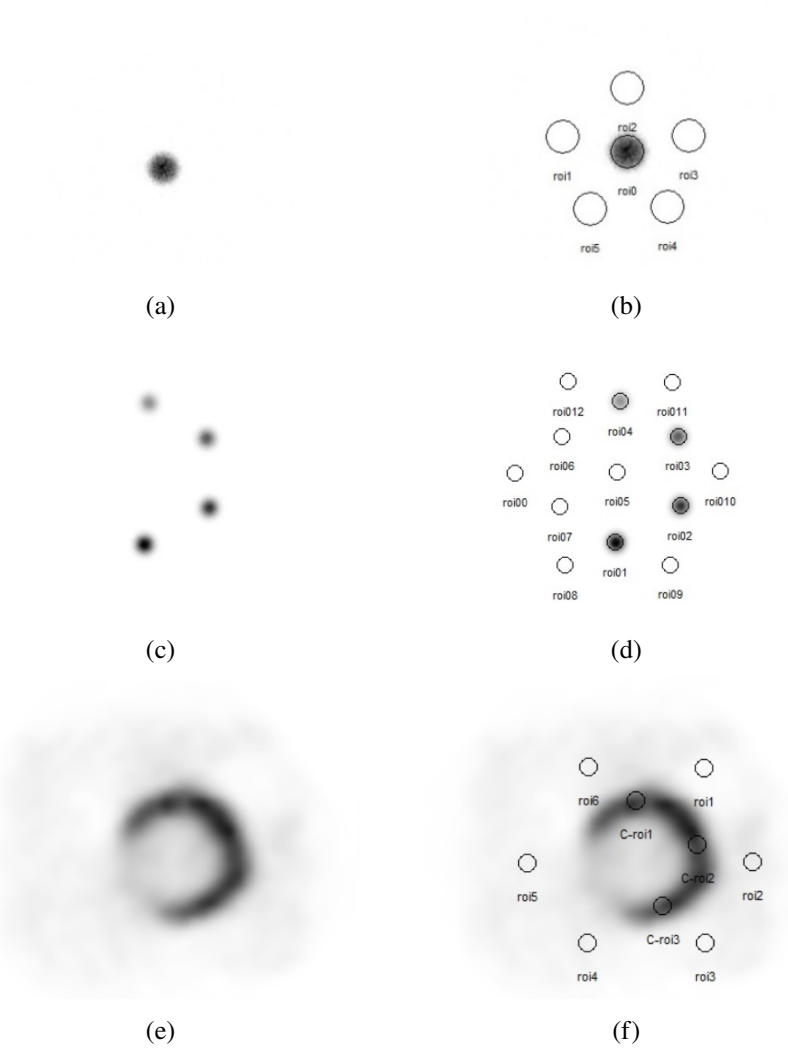
2023 JINST 18 P10009

2.5.2 Image contrast

Image contrast is the relative differences between count densities corresponding to the activity distributions of adjacent regions. As a result, contrast of an image is a measurement of how easily abnormal tissue may be distinguished from surrounding tissue [31]. Accordingly, the contrast parameter was calculated for both planar and SPECT images, as following equation:

$$\text{Contrast} = \frac{C_{\text{source}} - C_{\text{BG}}}{C_{\text{BG}}} \tag{2.4}$$

Where C_{source} (counts/pixel) is count read in the source ROIs and C_{BG} (counts/pixel) is the average count read in the BG ROIs. As an example, when the average C_{BG} was determined in figure 4(b), five BG ROIs were considered in equation (2.4).



(a) (b) (c) (d) (e) (f)

Figure 4. Planar images of Tc-99m filled sources within Jaszczak SPECT phantom and source-BG ROIs drew for (a–b) sphere, (c–d) four rods. SPECT images of Tc-99m filled cardiac phantom with (e) a short-axis slice from myocardial images (f) source-BG ROIs drew on the same image.

2023 JINST 18 P10009

2.5.3 Spatial resolution

Spatial resolution, one of the most significant image quality parameters, determines the extent to which detail and sharp edges in an image can be detected in an imaging system. It is mentioned that the spatial resolution is read from the full width at half maximum (FWHM) of the source profile, using the counts and position information of a row of pixels (called the profile) in the image that passing through the point source [6]. The profile curves obtained from the images are used to determine the FWHM parameter.

In the study, rectangular profile ROIs were drawn along the center of each circular ROI on sphere (figure 5(a)) and rods images, using the Xeleris® workstation. In a similar way, a profile ROI passed through the center of the myocardium was drawn in the short-axis slices of SPECT myocardial images (figure 5(b)). Examples of the profile curves obtained from these profile ROIs are shown in figure 5(c,d). Then, FWHM data were read from the profile curves.

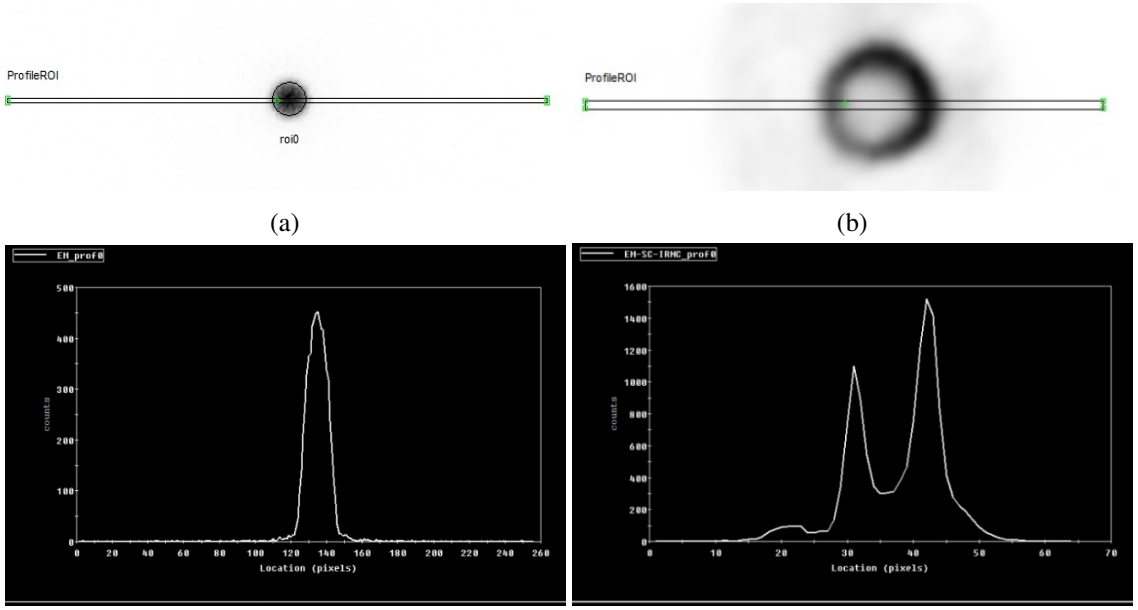


Figure 5. Profile ROI passed through the (a) center of the source ROI on the sphere image and (b) center of the myocardium on SPECT image, (c) profile curve of the sphere image, (d) profile curves of the myocardium image.

3 Results and discussion

3.1 Tc-99m energy spectrum

It is well known that the ^{99m}Tc photopeak (140 keV), iodine escape peak (112 keV) and characteristic X-ray peak (70–90 keV) appears in the ^{99m}Tc energy spectrum recorded with a traditional gamma camera system. It is mentioned that the photopeak is a representation of interactions, primarily photoelectric interactions, in which photon energy is practically completely transferred to the crystal [32]. Characteristic X-ray peaks are formed following the emission of characteristic lead X-rays produced by photoelectric interactions of the ^{99m}Tc photons with lead shielding and

2023 JINST 18 P10009

collimation [33]. The iodine escape peak occurs when the characteristic K-shell X-ray of iodine escapes from the crystal after the gamma-ray has undergone photoelectric absorption, measuring gamma-ray energy for ^{99m}Tc at 112 keV (140 minus 28 keV) [34].

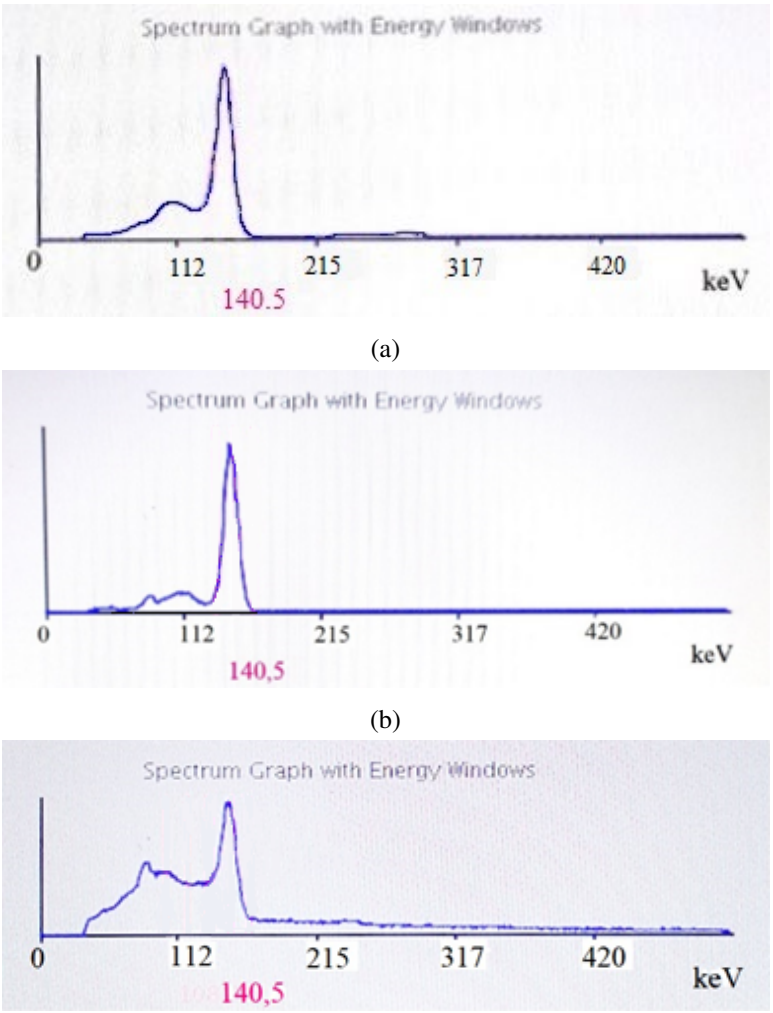


Figure 6. Acquired energy spectra of the (a) Tc-99m point source in the air without collimator, (b) Tc-99m point source in the air with the LEHR collimator, (c) Tc-99m sphere within the water-filled Jaszczak phantom with the LEHR collimator.

Tc-99m photopeak on 140 keV and iodine escape peak on 112 keV appeared on the spectra given in figure 6. As expected, the characteristic X-ray peaks are only seen in the spectra that were acquired with a collimator (figure 6(b,c)). If figure 6(b) is compared to figure 6(a), the scattered photon contributions on the Compton continuum in the spectra can be noticed. Namely, using the LEHR collimator prevents the scattered photons, reducing the Compton continuum. Moreover, the Compton continuum of the spectrum acquired with the water-filled Jaszczak phantom is higher than others because more photons are scattered in the scattering medium (figure 6(c)). Such that the iodine escape peak remains under the Compton continuum and is not observed.

2023 JINST 18 P10009

3.2 I-123 energy spectrum

As expected, the 159 keV of the ^{123}I photopeak and characteristic X-ray peak (70–90 keV) are seen in the ^{123}I energy spectrum acquired with the gamma camera system (figure 7). Energy spectra of the ^{123}I point source recorded in the air with LEHR, MEGP and HEGP collimator are given in figure 7(a–c), while figure 7(d) shows the acquired energy spectrum with LEHR collimator for the ^{123}I rod source within the water-filled Jaszczak phantom. It is noticed that the region on the right side of the photopeak in figure 7(a) is higher compared to the other spectra, due to the penetration of high-energy photons, as stated earlier. Furthermore, it is recognized that the area under the spectrum in figure 7(d) is larger as a result of the increased photon scattering events in the water medium.

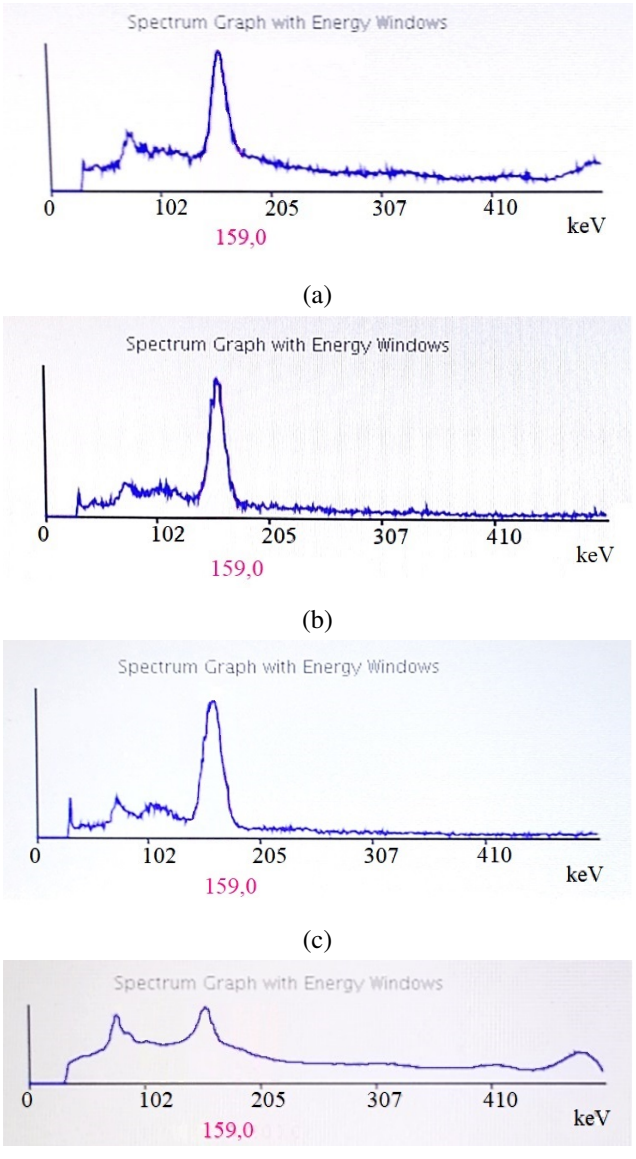


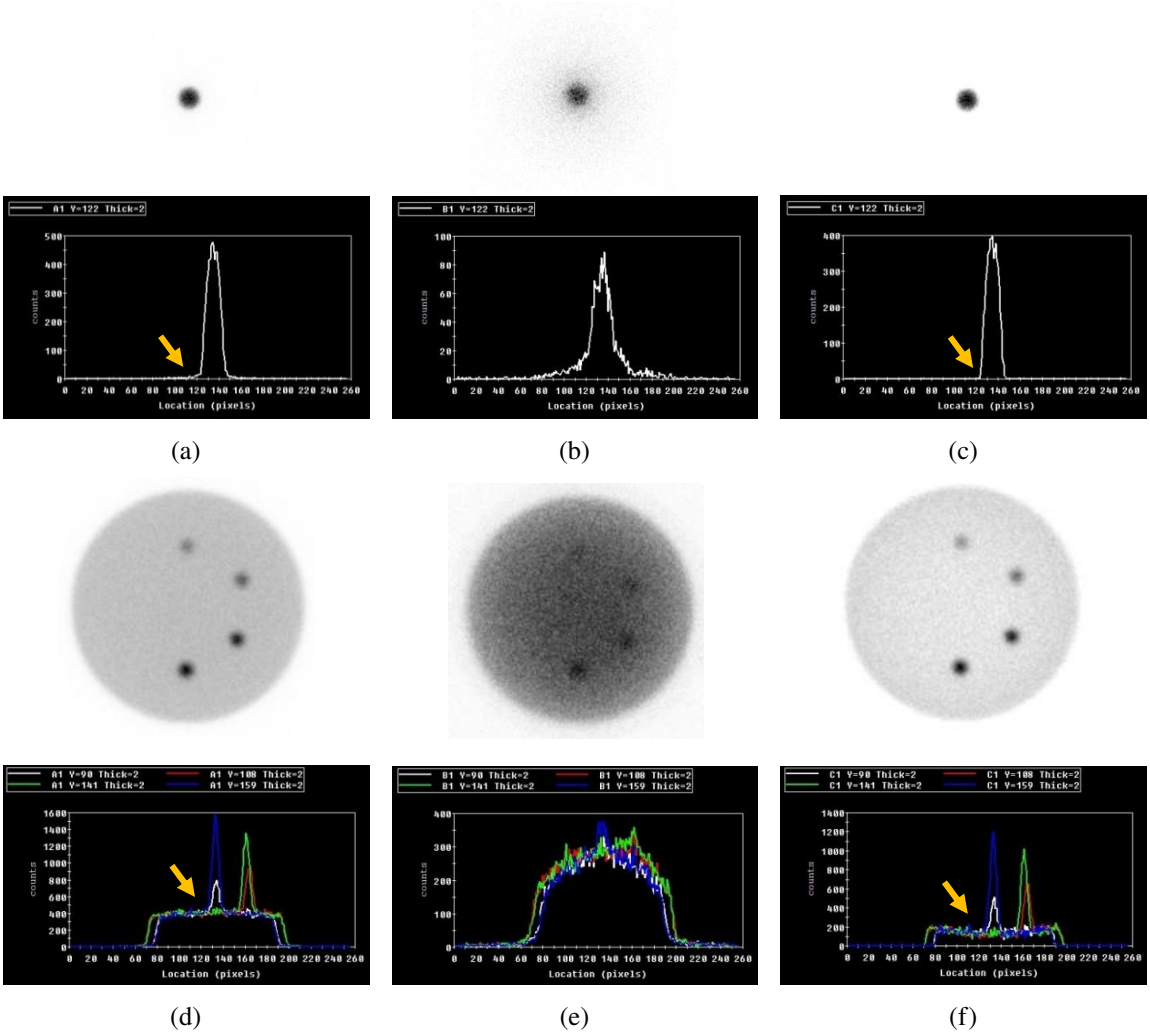
Figure 7. Acquired energy spectra of the I-123 point source in air with the (a) LEHR, (b) MEGP, (c) HEGP collimator, (d) I-123 rod source within the water-filled Jaszczak phantom with the LEHR collimator.

2023 JINST 18 P10009

3.3 Evaluation of DEW/TEW methods on planar imaging

3.3.1 Visual evaluations

In the study, DEW/TEW corrected and uncorrected phantom images were visually evaluated. Tc-99m planar images acquired using the photopeak and scatter windows for the sphere and rods and corresponding profile curves are shown in the first and middle columns of figure 8. Similarly, figure 9 shows the ^{123}I planar images acquired using the photopeak and corresponding profile curves for the sphere and rods. In addition, the last column of figure 8–9 presents the images that applied DEW and TEW correction methods with their corresponding profiles curves. Accordingly, the improvement of image quality is clearly seen in the sphere and rods images shown in figure 8(c, f) and figure 9(b, d). In particular, it is recognized that the edges of spheres and rods are more noticeable.



(a) (b) (c)

(d) (e) (f)

Figure 8. Planar images and profiles curves of the Tc-99m filled sphere and rod sources for (a,d) 126–154 keV of primary energy window and (b,e) 92–125 keV of scatter energy window, (c,f) applied DEW method. Orange arrows indicate the baseline of the profile curves.

2023 JINST 18 P10009

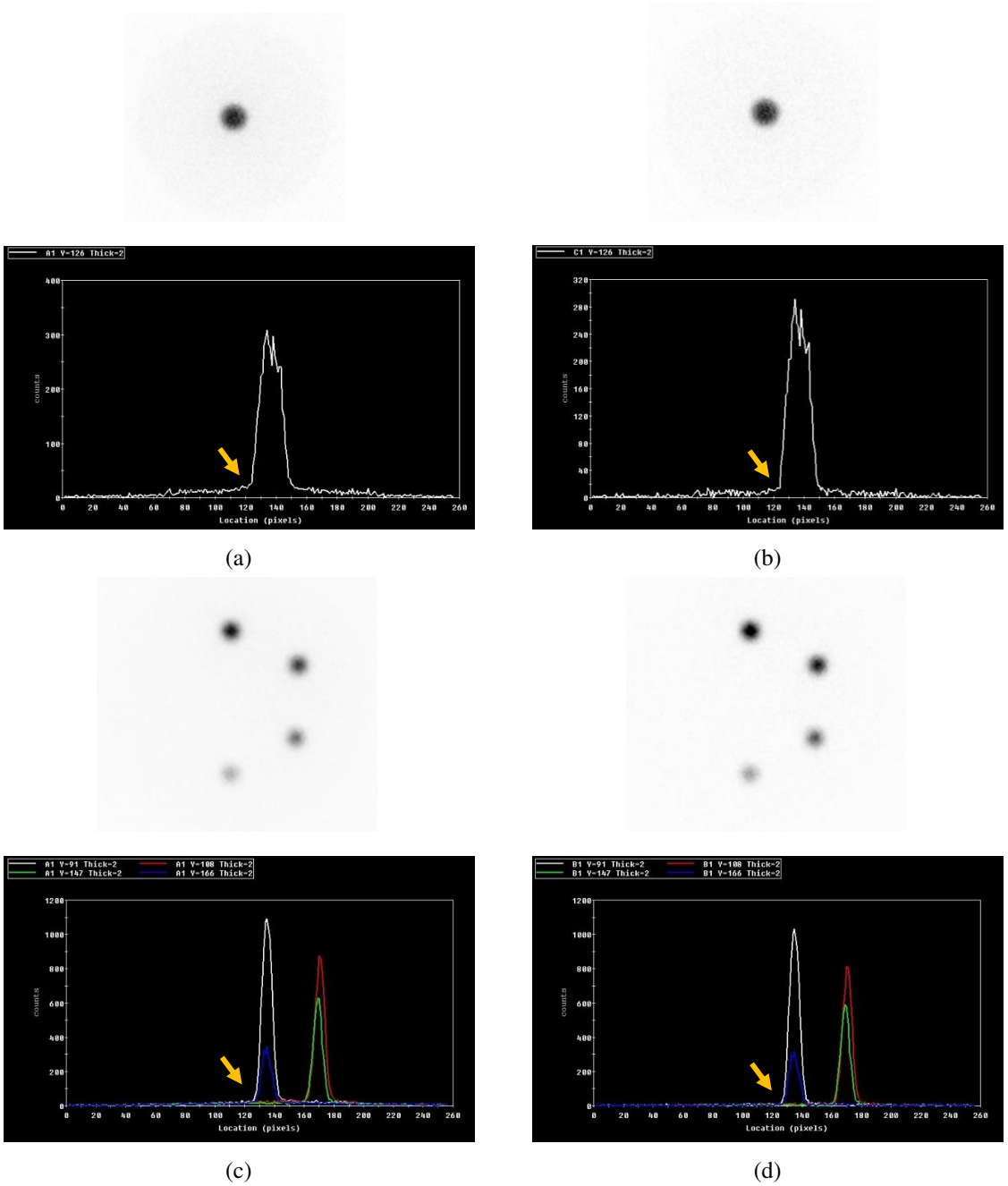


Figure 9. Planar images and profiles curves of the I-123 filled sphere and rod sources for (a,c) 147–170 keV of primary energy window, (b,d) applied TEW method. Orange arrows indicate the baseline of the profile curves.

3.3.2 Image quality parameters

Image contrast. The contrast was calculated for both scatter-corrected and uncorrected images, using equation (2.4). Figure 10–11 shows the contrast values of the planar sphere and rods images taken with the LEHR, MEGP, and HEGP collimators for different photopeak/scatter energy windows. It is clearly seen that the contrast of the scatter-corrected images is better than uncorrected ones, as

2023 JINST 18 P10009

mentioned by other studies [7, 10, 20, 25]. When the contrast data is compared, it is recognized that the scatter window with 92–125 keV gave the best ^{99m}Tc images (figure 10(a,c). The scatter windows of 136–146 keV and 173–185 keV resulted with the highest contrast in ^{123}I imaging (figure 11(a,c)). It is also noticed that image contrast improves as the scatter window expands in both ^{99m}Tc and ^{123}I imaging (figure 10–11(a,c)).

Spatial resolution. In the study, the spatial resolution parameter is considered as the FWHM parameter read from the profile curves, which have a Gaussian distribution. The profile curves through the slices from images of sphere and rods acquired with primary window, scatter window, and from DEW/TEW scatter corrected images are presented in figure 8–9. In these figures, it is clearly noticed that the baseline of the profile curves plotted for DEW and TEW scatter-corrected images has decreased, as indicated by the orange arrows.

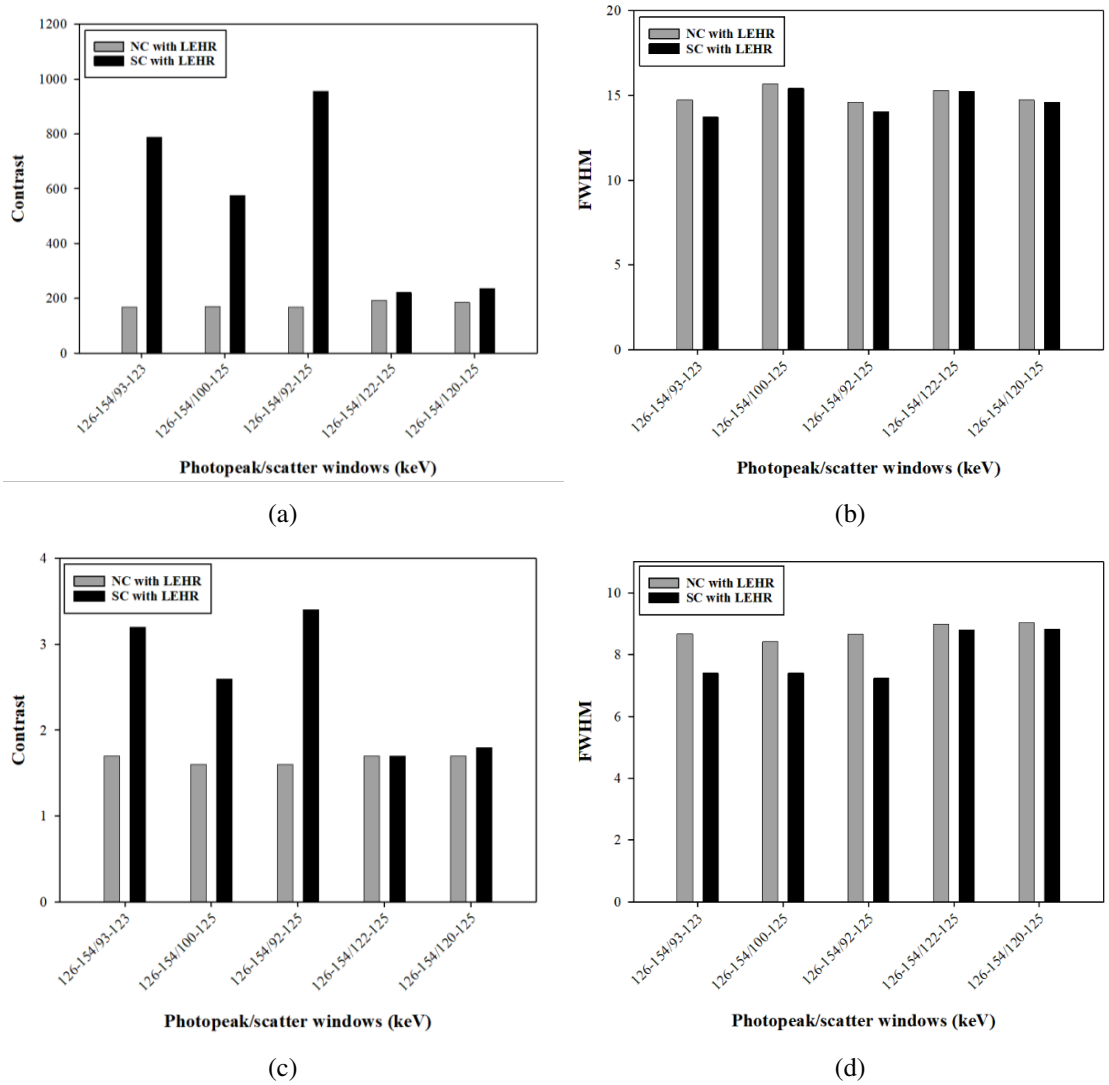


Figure 10. Variations of contrast and FWHM parameters of Tc-99m planar (a,b) sphere and (c,d) rod images acquired with different photopeak/scatter energy windows. NC: no corrected. SC: scatter corrected.

2023 JINST 18 P10009

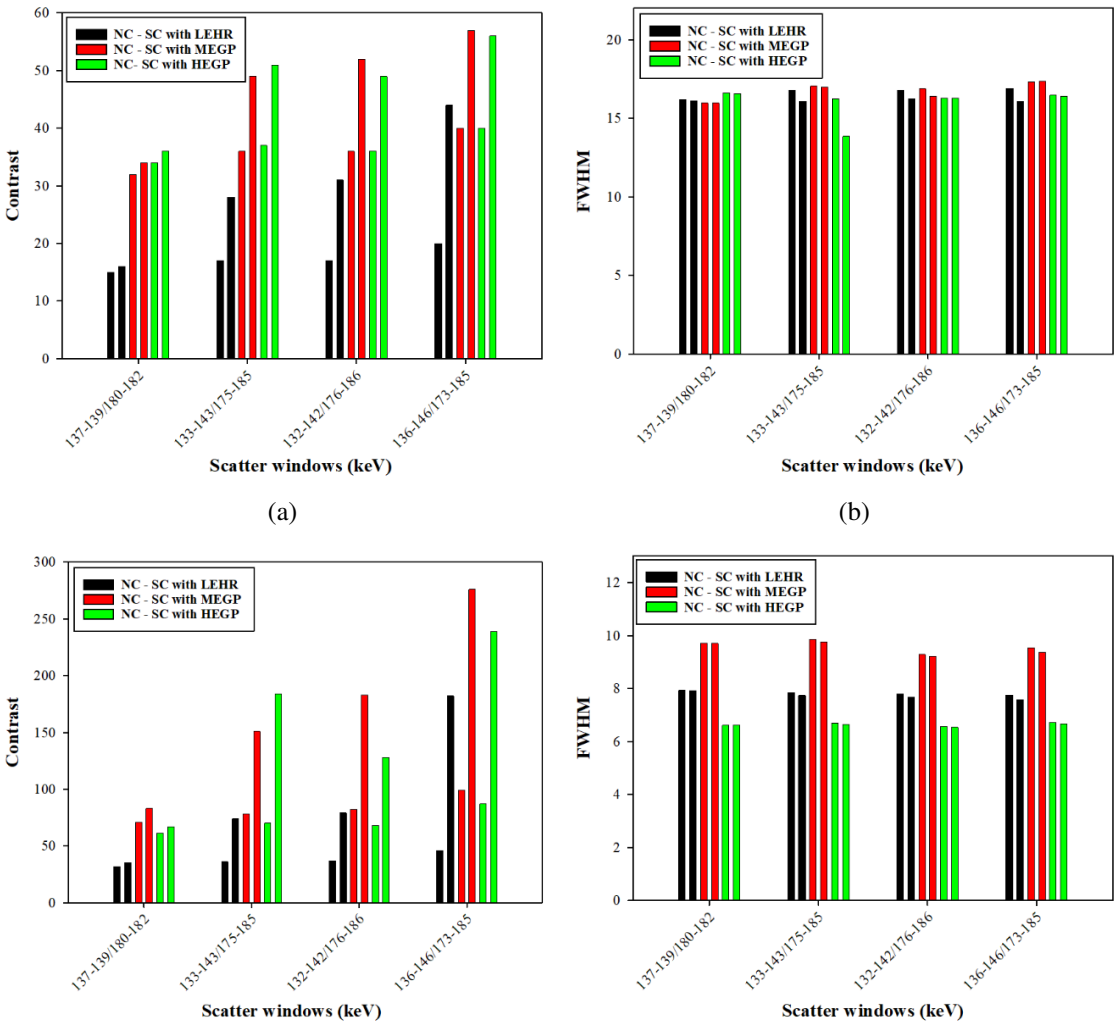


Figure 11. Variations of contrast and FWHM parameters for I-123 planar imaging acquired at 159 keV according to the left/right scatter energy windows for sources of (a,b) sphere and (c,d) rod. NC: no corrected. SC: scatter corrected.

The reported FWHM values read from the profile curves are an average based on the shape of the distribution data. The width of the distribution is a measure of the precision of the measurement as well. So, figure 10–11 shows the FWHM data for the planar (b) sphere and (d) rods images acquired with different photopeak/scatter windows. It is clearly seen from figure 10–11 that the FWHM parameters of the DEW and TEW scatter-corrected images are better than uncorrected ones. According to the measured data, the lowest FWHM is found for both sphere and rod ^{99m}Tc images acquired with scatter windows of 93–123 keV and 92–125 keV. In addition, wider scatter windows gave the best image with improved FWHM parameters.

2023 JINST 18 P10009

3.4 Evaluation of DEW/TEW methods on SPECT imaging

3.4.1 Visual evaluations

The DEW and TEW scatter corrections were visually evaluated by comparing the corrected and uncorrected SPECT images. The iterative reconstructed (IR) SPECT images of the sphere, rod and cardiac phantom without scatter correction are given in the first column of figure 12. In addition, the second column of figure 12 corresponds to images that applied the DEW correction method. The improvement of image quality is clearly seen in the phantom images. Namely, it is observed that the corrected images have a lower background uptake than the uncorrected ones. As seen in figure 12(b,d,f), the edges of the sphere, rods and myocardium are clearer.

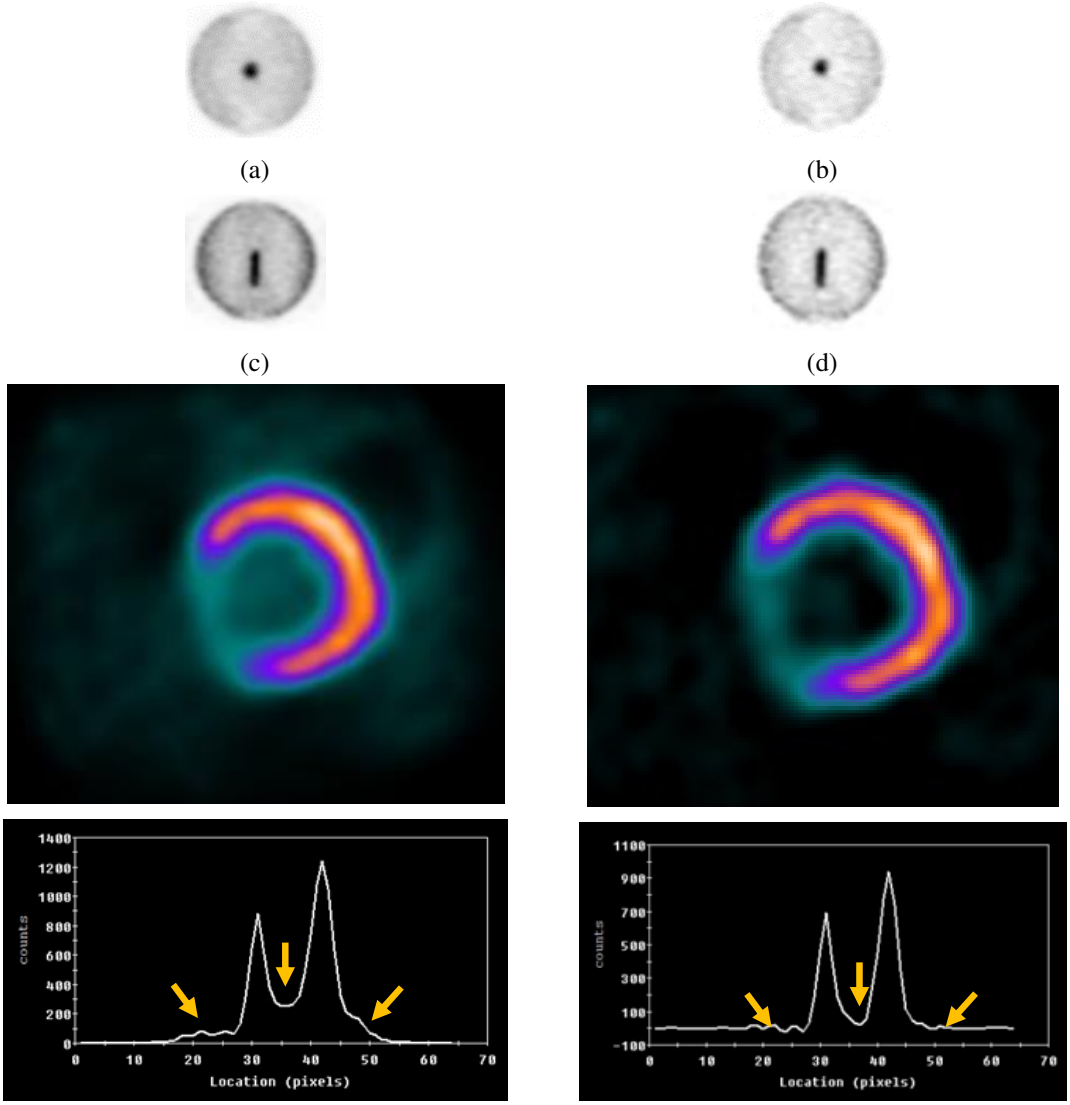


Figure 12. The slices of reconstructed SPECT sphere, rod, and myocardium images (a,c,e) without correction, (b,d,f) with applied DEW correction. The profile curves were obtained from the (e) uncorrected and (f) corrected myocardium images. Orange arrows indicate the baseline of the profile curve.

2023 JINST 18 P10009

3.4.2 Image quality parameters

Image contrast. The contrast was evaluated for IR SPECT images with and without DEW/TEW scatter corrections. Figure 13–14 shows the contrast values of the (a) sphere and (c) rod SPECT images acquired with different photopeak/scatter energy windows. Accordingly, the contrast of the scatter-corrected images is higher than the uncorrected ones. It can be also recognized that the scatter window of 92–125 keV had the highest contrast and gave the best ^{99m}Tc image. Among the calculated data, the highest contrast is found for both sphere and rod ^{123}I images acquired with scatter windows of 132–142 keV/176–186 keV and 136–146 keV/173–185 keV. As mentioned in planar imaging, image contrast improves as the scatter window expands in DEW and TEW corrected SPECT images, as well.

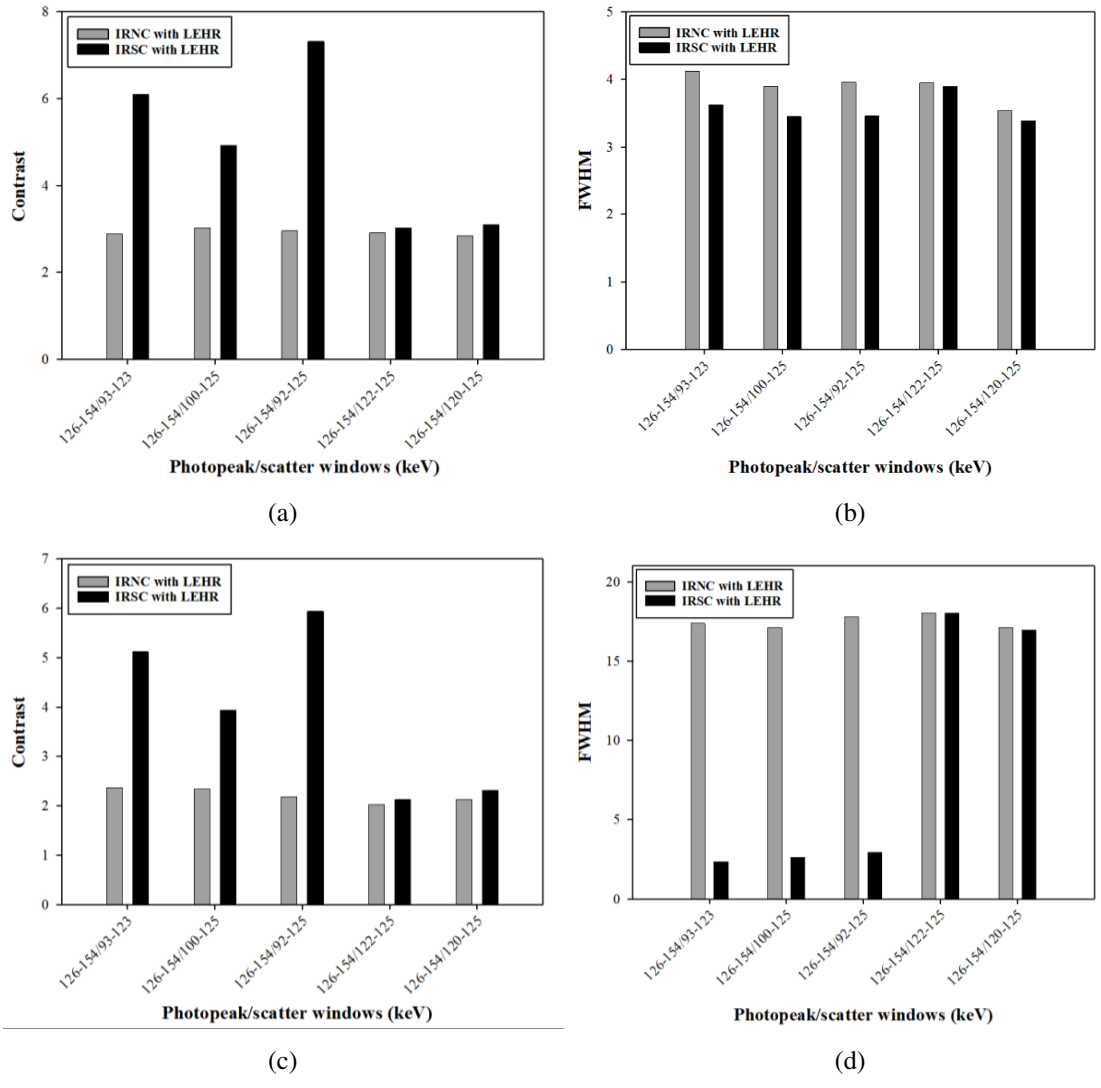


Figure 13. Variations of contrast and FWHM data of Tc-99m SPECT (a,b) sphere, (c,d) rod images acquired with different photopeak/scatter windows. IRNC: iterative reconstruction-no correction. IRSC: iterative reconstruction-scatter correction.

2023 JINST 18 P10009

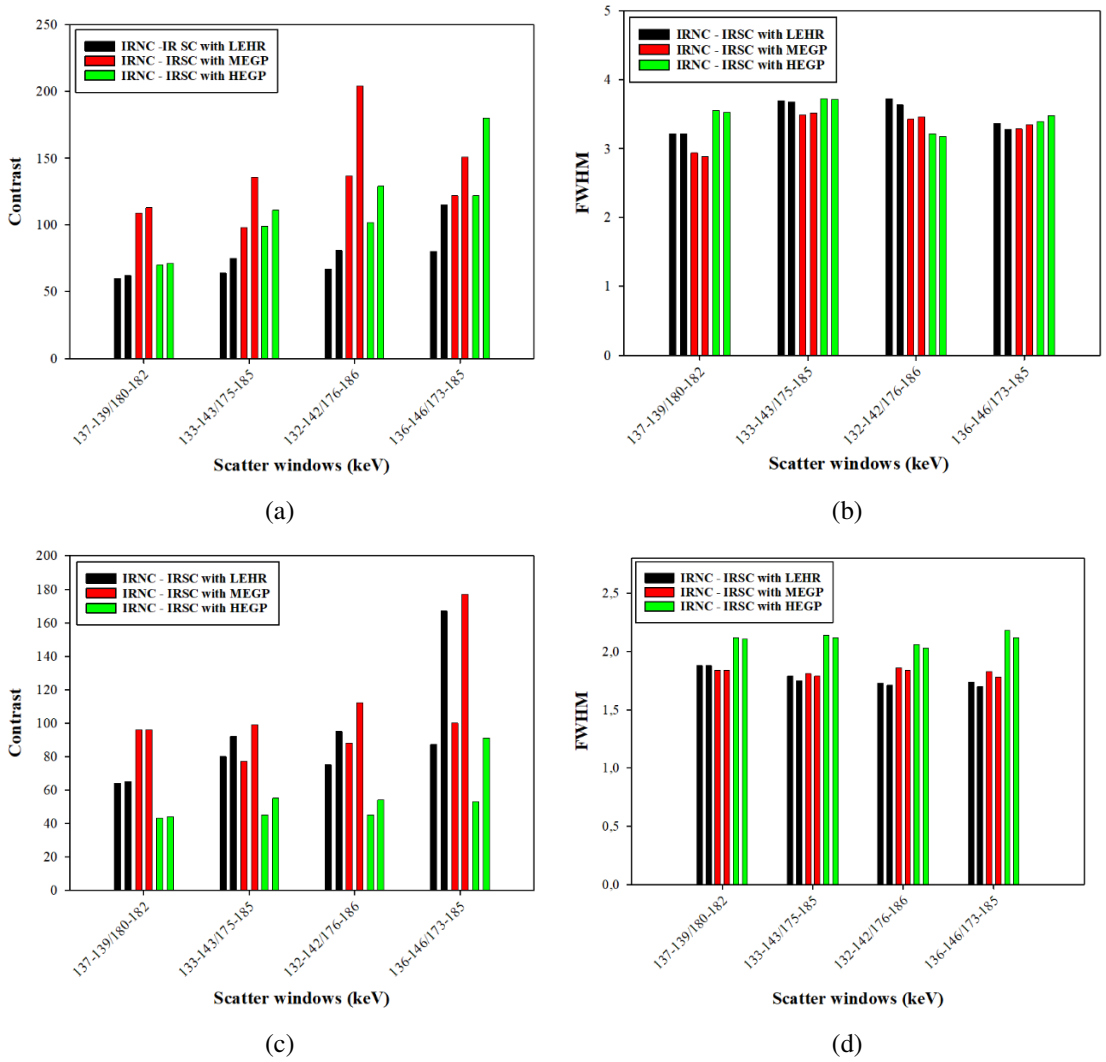


Figure 14. Variations of contrast and FWHM data for I-123 SPECT imaging acquired at 159 keV according to the left/right scatter energy windows for sources of (a,b) sphere, (c,d) rod. IRNC: iterative reconstruction-no correction. IRSC: iterative reconstruction-scatter correction.

Spatial resolution. The spatial resolution parameter is considered as the FWHM parameter read from the profile curves, similar to planar imaging. As an example of the profile curves in SPECT imaging, the profile curves for the slices of reconstructed SPECT myocardium images with and without DEW correction are presented in figure 12(e,f). It is clearly recognized that the baseline of the profile curves drops as the area contributed by the scattered photons decreases, as showed by the orange arrows (figure 12(e,f)).

Variations of the FWHM data for sphere and rod SPECT images acquired at different photo-peak/scatter windows are given in figure 13–14(b,d). It is clearly seen from these figures that the FWHM parameters of the DEW/TEW scatter-corrected SPECT images are better as compared to the uncorrected ones. Among the investigated scatter windows, the lowest FWHM value read from the profile curves is found for the scatter windows of 93–123 keV and 92–125 keV. Similar to the planar

2023 JINST 18 P10009

imaging, the DEW and TEW corrected SPECT images with wider scatter windows gave the best image with improved FWHM parameters.

4 Conclusion

In routinely performed ^{99m}Tc and ^{123}I imaging for diagnostic evaluation, the fact that Compton scattered photons carry misleading information about the photon's emission point is a factor affecting the image quality. For this reason, the methods aimed to decrease the effect of scattering are one of the most challenging issues in nuclear medicine.

The DEW and TEW scatter correction methods are widely used to reduce image defects caused by scattered photons. In this research, ^{99m}Tc/^{123}I planar and SPECT images were evaluated by image quality parameters of contrast and spatial resolution. When the image quality parameters of corrected and uncorrected images are compared, the DEW and TEW scatter correction methods improved image quality.

According to the findings of our phantom study on the DEW scatter correction method, it should be said that setting a 92–125 keV of scatter energy window during ^{99m}Tc acquisition results in the highest contrast and best spatial resolution on images. As for ^{123}I imaging, although the highest contrast and best spatial resolution vary depending on the collimator utilized, the best image was achieved by setting a 136–146/173–185 keV of scatter energy window.

Finally, as the scattering medium is greater in routine clinical imaging, further scatter correction studies based on ^{99m}Tc and ^{123}I imaging of patients must be performed for a more realistic evaluation.

Acknowledgments

Grateful thanks are offered to the provider of financial support for the research presented here: Dokuz Eylül University Scientific Research Project (Project no: 2020.KB.SAG.030). The authors are also grateful to Dr. Kamil Köseoğlu for professional advice on scatter correction methods, to Mr. Burak Akgül for his help in using GE Healthcare Xeleris® workstation, to the staff of Nuclear Medicine Department at Dokuz Eylül University for their collaboration during the measurements.

Declaration of competing interest. The authors declare that they have no known potential conflict of interest reported.

References

[1] J. O'Malley and H. Ziessman, *Nuclear Medicine and Molecular Imaging*, Elsevier, Philadelphia, U.S.A. (2021).

[2] A.A. Dobbeleir, A.S.E. Hambye and P.R. Franken, *Influence of methodology on the presence and extent of mismatching between 99mTc-MIBI and 123I-BMIPP in myocardial viability studies*, *J. Nucl. Med.* **40** (1999) 707.

[3] E. Papanastasiou, E. Moralidis and A. Siountas, *The effect of scatter correction on planar and tomographic semiquantitative 123I cardiac imaging. A phantom study*, *Hell. J. Nucl. Med.* **20** (2017) 154.

2023 JINST 18 P10009

[4] K. Ogawa, *Simulation study of triple-energy-window scatter correction in combined Tl-201, Tc-99m SPECT*, *Ann. Nucl. Med.* **8** (1994) 277.

[5] S.A. Larsson et al., *A novel phantom design for emission tomography enabling scatter- and attenuation-"free" single-photon emission tomography imaging*, *Eur. J. Nucl. Med.* **27** (2000) 131.

[6] M.M. Khalil, *Basic Sciences of Nuclear Medicine*, Springer, Heidelberg, Germany (2011).

[7] J. Jaszczak, E. Floyd and C. Craig, *Improved SPECT quantification using compensation for scattered photons*, *J. Nucl. Med.* **25** (1984) 893.

[8] K. Ogawa et al., *A practical method for position-dependent Compton-scatter correction in single photon emission CT*, *IEEE Trans. Med. Imag.* **10** (1991) 408.

[9] V. Lagerburg, R. de Nijs, S. Holm and C. Svarer, *A comparison of different energy window subtraction methods to correct for scatter and downscatter in I-123 SPECT imaging*, *Nucl. Med. Commun.* **33** (2012) 708.

[10] M. Noori-Asl and A. Bitarafan-Rajabi, *Simulation and patient studies of scatter correction in cardiac SPECT imaging*, *Iran. J. Med. Phys.* **16** (2019) 430.

[11] M. Tanaka, S. Uehara, A. Kojima and M. Matsumoto, *Monte Carlo simulation of energy spectra for ^{123}I imaging*, *Phys. Med. Biol.* **52** (2007) 4409.

[12] R. de Nijs et al., *Experimental determination of the weighting factor for the energy window subtraction-based downscatter correction for I-123 in brain SPECT studies*, *J. Med. Phys.* **35** (2010) 215.

[13] S. Shcherbinin, S. Chamoiseau and A. Celler, *Quantitative image reconstruction for dual-isotope parathyroid SPECT/CT: phantom experiments and sample patient studies*, *Phys. Med. Biol.* **57** (2012) 4755.

[14] A. Könik et al., *Primary, scatter, and penetration characterizations of parallel-hole and pinhole collimators for I-123 SPECT*, *Phys. Med. Biol.* **64** (2019) 245001.

[15] R. van Holen, S. Staelens and S. Vandenberghe, *SPECT imaging of high energy isotopes and isotopes with high energy contaminants with rotating slat collimators*, *Med. Phys.* **36** (2009) 4257.

[16] A.D. Small et al., *NOTE: Downscatter correction and choice of collimator in ^{123}I imaging*, *Phys. Med. Biol.* **51** (2006) N307.

[17] T. Ichihara, K. Ogawa, N. Motomura, A. Kubo and S. Hashimoto, *Compton scatter compensation using the triple-energy window method for single- and dual-isotope SPECT*, *J. Nucl. Med.* **34** (1993) 2216.

[18] I. Buvat, H. Benali, A. Todd-Pokropek and R.D. Paola, *Scatter correction in scintigraphy: the state of the art*, *Eur. J. Nucl. Med.* **21** (1994) 675.

[19] K. Nakajima et al., *Correction of iodine-123-labeled meta-iodobenzylguanidine uptake with multi-window methods for standardization of the heart-to-mediastinum ratio*, *J. Nucl. Cardiol.* **14** (2007) 843.

[20] E. Turan, *Application of the scatter correction techniques in the planar (Tl-201) imaging*, MSc Thesis Ege University, Turkey (2007), Turkish with English abstract.

[21] M. Noori-Asl, A. Sadremomtaz and A. Bitarafan-Rajabi, *Evaluation of six scatter correction methods based on spectral analysis in ^{99m}Tc SPECT imaging using SIMIND Monte Carlo simulation*, *J. Med. Phys.* **38** (2013) 189.

[22] M. Holstensson et al., *Model-based correction for scatter and tailing effects in simultaneous ^{99m}Tc and ^{123}I imaging for a CdZnTe cardiac SPECT camera*, *Phys. Med. Biol.* **60** (2015) 3045.

2023 JINST 18 P10009

[23] K.F. Koral, F.M. Swailem, S. Buchbinder, N.H. Clinthorne, W.L. Rogers and B.M.W. Tsui, *SPECT dual-energy-window Compton correction: Scatter multiplier required for quantification*, *J. Nucl. Med.* **31** (1990) 90.

[24] K. Perisinakis, N. Karkavitsas, J. Damilakis and N. Gourtsoyiannis, *Effect of dual and triple energy window scatter correction methods on image quality in liver scintigraphy*, *Nuklearmedizin* **37** (1998) 239.

[25] K. Köseoğlu, *Compton scatter correction methods based on spectral analysis in nuclear imaging*, Ph.D. Thesis Ege University, Turkey (2001), Turkish with English abstract.

[26] H. Kobayashi et al., *Scatter correction by two-window method standardizes cardiac I-123 MIBG uptake in various gamma camera systems*, *Ann. Nucl. Med.* **17** (2003) 309.

[27] Y.-W. Yang et al., *Evaluation of collimator choice and scatter correction on ^{123}I SPECT images*, *Nucl. Instrum. Meth. A* **584** (2008) 204.

[28] H.J. Verberne et al., *Influence of collimator choice and simulated clinical conditions on 123I-MIBG heart/mediastinum ratios: a phantom study*, *Eur. J. Nucl. Med.* **32** (2005) 1100.

[29] C. İnce, Ö. Karadeniz, T. Ertay and H. Durak, *Collimator and energy window optimization for YTTRIUM-90 bremsstrahlung SPECT imaging*, *Appl. Radiat. Isot.* **167** (2021) 109453.

[30] J.T. Bushberg, J.A. Seibert, E.M. Leidholdt and J.M. Boone, *The Essential Physics of Medical Imaging*, Lippincott Williams & Wilkins, Philadelphia, PA, U.S.A. (2012).

[31] G.B. Saha, *Physics and Radiobiology of Nuclear Medicine*, Springer Science+Business Media, New York, NY, U.S.A. (2013).

[32] D. Hamilton, *Diagnostic Nuclear Medicine*, Springer-Verlag Berlin Heidelberg, Berlin (2004).

[33] S.R. Cherry, J.A. Sorenson and M.E. Phelps, *Physics in Nuclear Medicine*, Saunders Elsevier Inc., Philadelphia, PA, U.S.A. (2012).

[34] F.A. Mettler and M.J. Guiberteau, *Essentials of Nuclear Medicine Imaging*, Saunders Elsevier Inc., China (2012).

[35] S.K. Gupta and V. Rangarajan, *Radiopharmaceutical Biodistribution and Dosimetry*, in *Radiopharmaceuticals — Current Research for Better Diagnosis and Therapy*, F.A. Badria, ed., IntechOpen (2022) [DOI:10.5772/intechopen.104917].

[36] K. Maher, *Chapter 9: Nuclear Medicine Imaging Systems*, in *Basic Physics of Nuclear Medicine*, WikiBooks (2008), https://en.wikibooks.org/wiki/Basic_Physics_of_Nuclear_Medicine/Nuclear_Medicine_Imaging_Systems.

2023 JINST 18 P10009